Chromium poisoning in (La,Sr)MnO3 cathode: Three-dimensional simulation of a solid oxide fuel cell

AUTHOR(S):

Miyoshi, Kota; Iwai, Hiroshi; Kishimoto, Masashi; Saito, Motohiro; Yoshida, Hideo

CITATION:

Miyoshi, Kota ...[et al]. Chromium poisoning in (La,Sr)MnO3 cathode: Three-dimensional simulation of a solid oxide fuel cell. Journal of Power Sources 2016, 326: 331-340

ISSUE DATE:

2016-09-15

URL:

http://hdl.handle.net/2433/218982

Chromium poisoning in (La,Sr)MnO_3 cathode: three-dimensional simulation of a solid oxide fuel cell

Kota Miyoshi[a], Hiroshi Iwai[a], Masashi Kishimoto[a], Motohiro Saito[a], Hideo Yoshida[a]

[a] Department of Aeronautics and Astronautics, Kyoto University, Kyoto 615-8540, Japan

Phone: +81 75 383 3652

Email address: miyoshikota@gmail.com

Abstract

A three-dimensional numerical model of a single solid oxide fuel cell (SOFC) considering chromium poisoning on the cathode side has been developed to investigate the evolution of the SOFC performance over long-term operation. The degradation model applied in the simulation describes the loss of the cathode electrochemical activity as a decrease in the active triple-phase boundary (TPB) length. The calculations are conducted for two types of cell: lanthanum strontium manganite (LSM)/yttria-stabilized zirconia (YSZ)/Ni-YSZ and LSM-YSZ/YSZ/Ni-YSZ. Their electrode microstructures are acquired by imaging with a focused ion beam scanning-electron microscope (FIB-SEM). The simulation results qualitatively reproduce the trends of chromium poisoning reported in the literature. It has been revealed that the performance degradation by

chromium is primarily due to an increase in the cathode activation overpotential. In addition, in the LSM-YSZ composite cathode, TPBs in the vicinity of the cathode–electrolyte interface preferentially deteriorate, shifting the active reaction site towards the cathode surface. This also results in an increase in the cathode ohmic loss associated with oxide ion conduction through the YSZ phase. The effects of the cell temperature, the partial pressure of steam at the chromium source, the cathode microstructure, and the cathode thickness on chromium poisoning are also discussed.

Keywords: Solid oxide fuel cells, Chromium poisoning, Triple phase boundary, Numerical simulation

1. Introduction

The performance degradation of solid oxide fuel cells (SOFCs) due to impurities is a critical issue that must be overcome for the commercialization of SOFC systems. Chromium, which is contained in the alloy separators and flow channel walls of SOFC systems, causes severe degradation in SOFC cathodes [1]. A number of experimental studies [2-9] and a thermodynamic analysis [10] have led to the proposal of the following two main reactions for chromium poisoning in lanthanum strontium manganite/yttria-stabilized zirconia (LSM-YSZ) cathodes.

$$2CrO_2(OH)_{2(g)} + 6e^- \rightarrow Cr_2O_{3(s)} + 2H_2O + 3O^{2-} \quad (1)$$

$$(La_{0.8}Sr_{0.2})MnO_3 + 0.1CrO_{3(g)} \rightarrow 1.1(La_{0.8}Sr_{0.2})_{0.909}(Mn_{0.909}Cr_{0.091})O_3 \quad (2)$$

Eq. (1) is an electrochemical reaction, where gaseous chromium in the supplied air is electrochemically reduced near the active reaction sites to form solid chromium oxide (III), covering up the reaction sites at which the electrochemical reduction reaction of oxygen can occur [9]. On the other hand, Eq. (2) is a chemical reaction, where chromium replaces manganese atoms in the B-site of the perovskite LSM crystal [10], which may reduce the electronic conductivity within the phase.

Konysheva et al. [5,6] reported the distribution of chromium in an LSM-YSZ composite cathode after exposure to chromium-containing air as observed by an energy-dispersive X-ray (EDX) mapping. Under open-circuit voltage (OCV) conditions, chromium was distributed randomly in the entire cathode, whereas under a current load of 200 mA cm^{-2}, chromium was detected in the vicinity of the cathode–electrolyte interface. In addition, the increase in the activation overpotential under a current load was significantly larger than that under OCV conditions. Horita et al. [9] reported a similar tendency in an LSM cathode; chromium deposition mainly occurred near the triple-phase boundary (TPB) region under a current load while a uniform chromium distribution was observed under OCV conditions. Most of the degradation in the cathode was found to be due to an increase in the activation overpotential, although a slight increase in the ohmic resistance was also observed. These findings indicate that the main factor causing degradation by chromium is not the chemical reaction between LSM and chromium but the electrochemical reaction of chromium oxide at the TPBs. In this case, higher activation overpotential may promote the deposition of chromium.

The deposited chromium oxide may block the diffusion pathways of reactant gas species to the electrode reaction sites, i.e, TPBs, and decrease the local exchange current density. Nakajo et al. [11] proposed a model that considers the decrease in the local exchange current density as a decrease in

the TPB length owing to the electrochemical reaction of chromium oxide in LSM-YSZ composite cathodes. In this model, the relative decrease in the TPB density is a function of the cathode activation overpotential. They applied this model to a one-dimensional (1D) macroscale simulation and investigated the changes in overall performance over 12,000 h of exposure to chromium.

To improve understanding of the chromium degradation in SOFC cathodes, microscale simulation using actual microstructure data for porous electrodes is useful. Recent developments in tomography techniques, such as imaging with a focused ion beam scanning electron microscope (FIB-SEM) and X-ray computed tomography (CT), enable us to directly observe and virtually reconstruct electrode microstructures, which can be used in microscale simulations. Numerical simulation is an effective approach not only for calculating the overall system performance but also for analyzing microscale phenomena inside complex porous electrodes. Because the microstructure of the electrodes has a significant effect on the cell performance, researchers have been investigating the relationships between the electrode microstructure and the electrochemical performance through experimental and numerical approaches [12-18].

In this study, a three-dimensional (3D) numerical model of an SOFC considering chromium

poisoning on the cathode side has been developed to investigate the evolution of the SOFC performance over long-term operation. As a model for the chromium poisoning in LSM and LSM-YSZ composite cathodes, an empirical relationship proposed by Nakajo et al. [11] is applied. The electrode microstructures are acquired by FIB-SEM imaging. The time evolution of the cathode electrochemical performances, such as the activation overpotential and ohmic loss, is investigated. Also, the effects of the cell temperature, the partial pressure of steam at the chromium source, the cathode microstructure, and the cathode thickness on chromium poisoning are discussed.

2. 3D microstructural data of electrodes

To conduct the microscale simulation, we acquired 3D data of actual electrode microstructures using an FIB-SEM. Since Konysheva et al. [5] reported that the chromium-induced degradation on LSM cathodes was faster than that on LSM-YSZ composite cathodes, we prepared not only an LSM cathode but also an LSM-YSZ composite cathode for comparative purposes. Commercial LSM and LSM-YSZ inks (Fuel Cell Materials, U.S.A.) were painted and sintered on YSZ disks (Tosoh, Japan) at 1150 ^{o}C for 5 h. The sintered cathodes were impregnated with epoxy resin (Struers, Denmark) under vacuum so that the pores could be distinguished from the solid phases in SEM imaging. In the FIB-SEM imaging, a cross-sectional surface was first exposed by FIB milling, which was then

imaged by SEM using an in-lens secondary electron detector. After the SEM imaging, the surface was milled by an FIB with an increment of 10 nm orders so that a new surface was exposed for the subsequent SEM imaging. By repeating such FIB milling and SEM imaging, a series of 2D SEM images was obtained. More details of the FIB-SEM imaging can be found elsewhere [15]. Regions were selected for microstructural analysis and were subjected to the following image processing using Avizo software (FEI, U.S.A.): (i) alignment of the stack of images, (ii) noise reduction, and (iii) segmentation. More details can be found elsewhere [19,20]. Then, the 3D porous microstructure was virtually reconstructed, from which various microstructural parameters were quantified. For the Ni-YSZ anode, the results reported by Kishimoto et al. [17] were used. Quantification of the electrode microstructures was performed using the methods proposed by Iwai et al. [15]. Table 1 summarizes the microstructural parameters of the LSM cathode, LSM-YSZ composite cathode, and Ni-YSZ composite anode.

3. Numerical model

The simulation is based on the finite volume method (FVM), where the conservation of electrons, ions, and gas species is considered. The electrochemical reaction is assumed to take place only at the TPBs. In this model, the local transport coefficients in each grid $\Gamma_i^{\mathrm{eff,local}}$ are evaluated as

$$\Gamma_i^{\mathrm{eff,local}} = V_i^{\mathrm{local}} \Gamma_i^{\mathrm{bulk}}, \tag{3}$$

where V_i is the volume fraction of phase i in the grid. Details of the model were reported by Kishimoto et al. [16,17].

3.1 Calculation domains

The calculation domains in this study are LSM/YSZ/Ni-YSZ and LSM-YSZ/YSZ/Ni-YSZ single cells (Fig. 1). The *x* axis in Fig. 1 corresponds to the thickness direction of the cell. The anode and cathode have the 3D reconstructed microstructures obtained by FIB-SEM imaging, while the electrolyte is assumed to be a flat plate with a thickness of 8 μm. The microstructure is divided into grid elements, each of which contains a number of image voxels obtained from the FIB-SEM imaging. Table 2 summarizes information on the grid systems used in the numerical simulation. Using the sub-grid-scale (SGS) model developed by Kishimoto et al. [16,17], conservation of the phase volume is considered in each grid element, on the basis of which the effective transport coefficients of each chemical species are evaluated. In the composite electrode microstructure, TPBs are distributed within the entire 3D cathode structure, while in the LSM cathode they exist only on the 2D LSM–YSZ interface. The temperature is assumed to be constant and uniform in the whole of

the calculation domains.

3.2 Gas diffusion

The conservation of gas species i is expressed using the molar flux N_i and source term s_i as

$$\nabla \cdot N_i = s_i. \tag{4}$$

The dusty-gas model is used to evaluate the gas diffusion flux in the porous electrodes [21]:

$$\frac{N_i}{D_{i,\mathrm{K}}^{\mathrm{eff}}} + \sum_{j=1, j\neq i}^{n} \frac{X_j N_i - X_i N_j}{D_{ij}^{\mathrm{eff}}} = -\frac{P_{\mathrm{t}}}{RT}\nabla X_i - \frac{X_i}{RT}\left(1 + \frac{KP_{\mathrm{t}}}{\mu D_{i,\mathrm{K}}^{\mathrm{eff}}}\right)\nabla P_t, \tag{5}$$

where X_i and P_i are the molar fraction and partial pressure of gas species i, respectively, and P_t is the total pressure. μ and K are the mixture viscosity and permeability, respectively. $D_{i,\mathrm{K}}^{\mathrm{eff}}$ and D_{ij}^{eff} are the effective Knudsen diffusion coefficients and the effective binary diffusion coefficients [17], respectively. Assuming that the total pressure gradient is negligible, the second term of the right-hand side is ignored in this study.

The source term s_i is given by the electrochemical reaction at TPBs as follows:

Cathode side

$$s_{O_2} = \frac{i_{ct}}{4F}, \quad s_{N_2} = 0, \tag{6}$$

Anode side

$$s_{H_2} = -\frac{i_{ct}}{2F}, \quad s_{H_2O} = \frac{i_{ct}}{2F}, \tag{7}$$

where F is the Faraday constant and i_{ct} is the charge-transfer current density associated with the electrochemical reaction in the electrodes.

3.3 Electron and ion diffusion

The conservation of electrons and ions is expressed using electrochemical potentials as

$$\nabla \cdot \left(\frac{\sigma_{e^-}^{eff}}{F} \nabla \tilde{\mu}_{e^-} \right) = -i_{ct}, \tag{8}$$

$$\nabla \cdot \left(\frac{\sigma_{O^{2-}}^{eff}}{2F} \nabla \tilde{\mu}_{O^{2-}} \right) = i_{ct}, \tag{9}$$

where $\tilde{\mu}_{e^-}$ and $\tilde{\mu}_{O^{2-}}$ are the electrochemical potential of electrons and oxide ions, respectively. $\sigma_{e^-}^{eff}$ and $\sigma_{O^{2-}}^{eff}$ are the effective electronic and ionic conductivity, respectively. In this model, both

LSM and YSZ are considered to be mixed conductors, while Ni is considered to be a pure electron conductor. The bulk conductivities are given as follows:

LSM phase [22,23]

$$\sigma_{e^-} = \frac{4.2\times10^7}{T}\exp\left(\frac{-1200}{T}\right), \tag{10}$$

$$\sigma_{o^{2-}} = 4.0\times10^{-6}, \tag{11}$$

YSZ phase [24,25]

$$\sigma_{e^-} = \max\left(\begin{matrix}1.31\times10^9\exp\left(\frac{-4.52\times10^4}{T}\right)\left(\frac{P_{O_2,YSZ}}{101325}\right)^{-\frac{1}{4}},\\ 2.35\times10^4\exp\left(\frac{-1.94\times10^4}{T}\right)\left(\frac{P_{O_2,YSZ}}{101325}\right)^{\frac{1}{4}}\end{matrix}\right), \tag{12}$$

$$\sigma_{o^{2-}} = 3.40\times10^{-4}\exp\left(\frac{-10350}{T}\right), \tag{13}$$

Ni phase [26,27]

$$\sigma_{e^-} = 3.27\times10^6 - 1065.3T, \tag{14}$$

where $P_{O_2,YSZ}$ is the local partial pressure of oxygen in the YSZ phase and can be estimated from the electrochemical potentials as follows by assuming local thermodynamic equilibrium:

$$\tilde{\mu}_{o^{2-}} - 2\tilde{\mu}_{e^-} = \frac{1}{2}RT\ln\frac{P_{O_2,YSZ}}{10^5}. \tag{15}$$

3.4 Electrochemical reaction

The charge transfer current density i_{ct}, which is associated with oxygen reduction in the cathode or hydrogen oxidation in the anode, is evaluated by the following Butler–Volmer-type equation:

Cathode side [28]

$$i_{\mathrm{ct}} = i_{0,\mathrm{cat}} l_{\mathrm{TPB}} \left[\exp\left(\frac{2.0F}{RT}\eta_{\mathrm{act,cat}}\right) - \exp\left(-\frac{2.0F}{RT}\eta_{\mathrm{act,cat}}\right)\right], \tag{16}$$

Anode side [29]

$$i_{\mathrm{ct}} = i_{0,\mathrm{ano}} l_{\mathrm{TPB}} \left[\exp\left(\frac{2.0F}{RT}\eta_{\mathrm{act,ano}}\right) - \exp\left(-\frac{F}{RT}\eta_{\mathrm{act,ano}}\right)\right], \tag{17}$$

where l_{TPB} is the TPB density, $i_{0,\mathrm{cat}}$ and $i_{0,\mathrm{ano}}$ are the exchange current density per unit TPB length for the cathode and anode, respectively, and η_{act} is the local activation overpotential. For $i_{0,\mathrm{cat}}$ and $i_{0,\mathrm{ano}}$, the following empirical formulas are used:

Cathode side [18]

$$i_{0,\mathrm{cat}} = 2.14 \times 10^5 P_{\mathrm{O_2}}^{0.376} \exp\left(\frac{-29200}{T}\right), \tag{18}$$

Anode side [30]

$$i_{0,\mathrm{ano}} = 31.4 P_{\mathrm{H_2}}^{-0.03} P_{\mathrm{H_2O}}^{0.4} \exp\left(-\frac{18300}{T}\right), \tag{19}$$

The activation overpotential η_{act} is expressed as follows:

Cathode side

$$\eta_{\mathrm{act,cat}} = -\frac{1}{2F}\left(2\tilde{\mu}_{\mathrm{e}^-} - \tilde{\mu}_{\mathrm{O}^{2-}} + \frac{1}{2}RT\ln\frac{{P_{\mathrm{O}_2}}^{\mathrm{in}}}{10^5}\right) - \eta_{\mathrm{con,cat}}, \tag{20}$$

Anode side

$$\eta_{\mathrm{act,ano}} = \frac{1}{2F}\left(\tilde{\mu}_{\mathrm{O}^{2-}} - 2\tilde{\mu}_{\mathrm{e}^-} - \Delta G^0_{\mathrm{H_2O}} - RT\ln\frac{{P_{\mathrm{H_2O}}}^{\mathrm{in}}}{{P_{\mathrm{H_2}}}^{\mathrm{in}}}\right) - \eta_{\mathrm{con,ano}}, \tag{21}$$

where ${P_i}^{\mathrm{in}}$ is the bulk partial pressure of species i on the electrode surface and η_{con} is the concentration overpotential. The concentration overpotential, η_{con} is expressed as follows:

Cathode side

$$\eta_{\mathrm{con,cat}} = \frac{RT}{4F}\ln\frac{P_{\mathrm{O}_2}}{{P_{\mathrm{O}_2}}^{\mathrm{in}}}, \tag{22}$$

Anode side

$$\eta_{\mathrm{con,ano}} = \frac{RT}{2F}\ln\frac{{P_{\mathrm{H}_2}}^{\mathrm{in}}}{P_{\mathrm{H}_2}}\frac{P_{\mathrm{H_2O}}}{{P_{\mathrm{H_2O}}}^{\mathrm{in}}}. \tag{23}$$

3.5 Model of degradation by chromium

3.5.1 Partial pressure of chromium vapor

Various chromium compounds can be volatilized from the chromium source, such as Cr_2O_3, in the presence of steam at elevated temperatures. From the results of thermodynamic analysis, $CrO_2(OH)_2$ is considered to have the largest partial pressure in equilibrium with Cr_2O_3, which can be determined from the partial pressure of steam at the chromium source $P_{\mathrm{H_2O,Cr\ source}}$ and the temperature as reported in Hilpert et al. [31]. Therefore, we derived an approximate equation for $P_{\mathrm{CrO_2(OH)_2}}$ as a function of $P_{\mathrm{H_2O,Cr\ source}}$ and T with an Arrhenius-type formula by fitting the reported values using the least-squares method as follows:

$$P_{\mathrm{CrO_2(OH)_2}} = 2.26 \times 10^{-2}\, {P_{\mathrm{H_2O,Cr\ source}}}^{0.992} \exp\left(\frac{-6.70\times10^4}{RT}\right). \quad (24)$$

The thermodynamic data of the gaseous species used in the calculation by Hilpert et al. are obtained from the databases provided by Eddinghaus [32]. In this study, $P_{\mathrm{H_2O,Cr\ source}}$ and T on the cathode side are assumed to be constant and uniform. Therefore, $P_{\mathrm{CrO_2(OH)_2}}$ is also assumed to be constant and uniform.

3.5.2 Kinetic model of chromium poisoning

For the simulation of chromium poisoning in SOFC cathodes, a kinetic model is required to evaluate the chromium deposition as a function of local chemical and electrochemical properties, such as temperature, chromium vapor pressure and activation overpotential. Understanding of the elementary reaction steps in the overall chromium reduction reaction is necessary for the accurate kinetic model; however, to the authors' knowledge, there is no study to reveal them. On the other hand, Nakajo et al. [11] proposed a simple model of chromium poisoning by simplifying the deposition reaction into a single electrochemically-driven process. In their study, 1D degradation simulation of a single anode-supported cell considering chromium poisoning was conducted and compared with the experimental results of anode-supported cell stack that was operated over 3000 hours by de Haart et al. [33]. Although the results obtained by the model did not show perfect agreement in terms of the cell performance drop, the trend of the degradation was qualitatively reproduced. In this study, we applied this model directly to the 3D numerical simulation relying on this reproducibility, and investigated how the degradation proceeds inside the real cathode microstructure obtained by FIB-SEM.

In the proposed degradation model, chromium oxide is assumed to be deposited at TPBs through the electrochemical reaction expressed by Eq. (1). From this reaction, the chromium oxide deposited

on TPBs reduces the local exchange current density. Other species of chromium vapor, such as CrO_3, are ignored because of their smaller partial pressure than that of $CrO_2(OH)_2$. For instance, the thermodynamic calculation by Chen et al. [8] indicates that the partial pressure of CrO_3 is less than 2% of that of $CrO_2(OH)_2$ at 900 °C ($P_{CrO_3} = 1.4 \times 10^{-3}$, $P_{CrO_2(OH)_2} = 9.2 \times 10^{-2}$ Pa).

The charge-transfer current density associated with the above chromium oxide deposition reaction i_D is evaluated from the following Butler–Volmer-type equation:

$$i_D = i_{0,D} x_{CrO_2(OH)_2}^{0.5} x_{H_2O,Cr\ source}^{0.5} 2\sinh\left(\frac{F}{2RT}\eta_{act,cat}\right), \quad (25)$$

where x_i is the molar fraction of species i. This indicates that higher chromium and steam vapor pressures, a lower temperature, and a higher activation overpotential cause faster degradation. In accordance with the results of Horita et al. [9], $i_{0,D}$ is defined as 6.74 A m^{-2}. Since the contribution of the charge-transfer current associated with the chromium deposition reaction i_D to the total charge-transfer current at TPBs i_{ct}, is no more than 0.00002%, i_D is neglected in the calculation of the electrochemical potentials (Eqs. (8) and (9)) and is only used to obtain the relative decrease in the TPB density explained below. Since the consumption rate of chromium was no more than 4% of

supply rate in our calculation condition, we assumed that the chromium diffusion, Knudsen and molecular diffusion, is negligible and the partial pressure of chromium was constant and uniform within the entire cathode. Then, we also assumed constant total pressure. However, we have to note that this assumption can bring errors in concentration overpotential since the conservation law does not hold strictly. Bertei et al. [34] revealed that the anode concentration overpotential was overestimated when the uniform total pressure was assumed in H_2-H_2O-N_2 systems. This was remarkable when the H_2 and N_2 partial pressures were precisely solved, and H_2O partial pressure was estimated from the Graham's law under the assumption of the uniform total pressure. In our study, the simulation was conducted in the cathode side, where O_2 partial pressure was precisely solved and N_2 partial pressure was estimated from the Graham's law under the assumption of the uniform total pressure and uniform chromium vapor pressure. This might have introduced errors in the estimation of concentration overpotential since the conservation law does not hold strictly. Here, we would like to note that since the gradient of total pressure is negligible, the errors can be limited. Moreover, the contribution of the concentration overpotential is significantly small in the total overpotential. Therefore the errors in the concentration overpotential should not significantly alter the overpotential characteristics.

Nakajo et al. [11] modeled the degradation of local electrochemical activity due to chromium oxide deposition as a decrease in the TPB density as follows:

$$\frac{1}{A_{\mathrm{TPB}}}\frac{\partial A_{\mathrm{TPB}}}{\partial t} = -\frac{M_{\mathrm{Cr_2O_3}}}{6F\rho_{\mathrm{Cr_2O_3}}h_{\mathrm{TPB}}}i_{\mathrm{D}}, \tag{26}$$

where h_{TPB} is the maximum height of chromium oxide deposition, when the electrochemical reaction no longer proceeds at the TPBs and was set to 35 nm. This value was chosen from Konysheva et al. [6]. $M_{\mathrm{Cr_2O_3}}$ and $\rho_{\mathrm{Cr_2O_3}}$ is molecular weight and density of chromium oxide, respectively. Since Nakajo et al. assumed that the TPB had some width, they adopted TPB area A_{TPB}. Even though the relationship between the chromium deposition rate $\frac{M_{\mathrm{Cr_2O_3}}}{6F\rho_{\mathrm{Cr_2O_3}}}i_{\mathrm{D}}$ and the relative decrease in A_{TPB} is complex, Nakajo et al. assumed that the relative decrease in A_{TPB} is inverse proportional to h_{TPB} to obtain Eq. (26). Since A_{TPB} is the product of l_{TPB} and a certain constant width of TPB, eq. (26) can also be rewritten as follows to explicitly describe the relative decrease of l_{TPB}.

$$\frac{1}{l_{\mathrm{TPB}}}\frac{\partial l_{\mathrm{TPB}}}{\partial t} = -\frac{M_{\mathrm{Cr_2O_3}}}{6F\rho_{\mathrm{Cr_2O_3}}h_{\mathrm{TPB}}}i_{\mathrm{D}}, \tag{27}$$

The reverse reaction is not allowed in this model. Eq. (27) can be integrated to obtain

$$l_{\mathrm{TPB}}(t) = l_{\mathrm{TPB}}(0)\exp\left(-\int_0^t \frac{M_{\mathrm{Cr_2O_3}}}{6F\rho_{\mathrm{Cr_2O_3}}h_{\mathrm{TPB}}} i_{\mathrm{D}}\mathrm{d}t\right), \tag{28}$$

which is then discretized as follows:

$$l_{\mathrm{TPB}}(t_n) = l_{\mathrm{TPB}}(t_{n-1})\exp\left(-\frac{M_{\mathrm{Cr_2O_3}}}{6F\rho_{\mathrm{Cr_2O_3}}h_{\mathrm{TPB}}} i_{0,\mathrm{D}} x_{\mathrm{CrO_2(OH)_2}}^{0.5} x_{\mathrm{H_2O,Cr\ source}}^{0.5} 2\sinh\left(\frac{F\eta_{\mathrm{act,cat}}(t_{n-1})}{2RT}\right)\Delta t\right). \tag{29}$$

In this study, $l_{\mathrm{TPB}}(t_n)$ is calculated explicitly with a time span of Δt=250 h, using $l_{\mathrm{TPB}}(t_{n-1})$ and $\eta_{\mathrm{act,cat}}(t_{n-1})$ by assuming that the transport of the gas, electrons, and ions is in the steady state while chromium poisoning proceeds with time.

3.6 Procedure of numerical simulation

The numerical simulation of chromium poisoning is conducted as follows, as also shown in Fig. 2:

(i) Set the initial l_{TPB}.

(ii) Conduct the 3D simulation.

(iii) Obtain local activation overpotentials in all grids.

(iv) Calculate the local relative decrease in the TPB density with Eq. (29) and update the TPB density.

(v) Repeat the steps (ii) - (iv) until the time reaches the maximum value ($t_{\max} = 1500$ h).

The boundary conditions for the simulation are shown in Table 3. Here L_{Total} is the total cell thickness in the x direction and V_{t} is the terminal voltage. L_{Total} is 42.2 for the LSM cathode and 30.8 μm for the LSM-YSZ composite cathode.

4. Results and discussion

4.1 Degradation of electrochemical performance

Table 4 shows the calculation conditions in this study. All calculations were conducted under a 200 mA cm^{-2} current load with an anode gas of 97% H_2-3% H_2O and a cathode gas of 21% O_2-79% N_2. In Cases 1-4, the simulation was conducted for the LSM-YSZ composite cathode with different cell temperatures (750 and 850 ^{o}C) and molar fractions of steam at the chromium source (0.1 and 2.6%). These results were used to investigate the effects of temperature as well as the partial pressure of $CrO_2(OH)_2$ in the cathode gas. In Cases 5 and 6, the simulation was conducted for the LSM

cathode at different temperatures (750 and 850 ºC) with a wet chromium source. By comparing the results of Cases 1 and 2 with those of Cases 5 and 6, the effects of the microstructure were investigated. In Cases 7 and 8, the simulation was conducted for the LSM-YSZ composite cathode with different thicknesses (7.0 and 13 μm) to investigate the effect of thickness.

In this subsection, simulation results for the LSM-YSZ composite cathode with a steam molar fraction of 2.6% and a wet chromium source at 850 ºC (Case 1) are discussed. Fig. 3 shows the evolution of the voltage losses in the cell. It is found that the degradation due to chromium is mainly caused by an increase in the cathode activation overpotential, which is consistent with the experimental results in the literature [2-9]. Also, a slight increase in the cathode ohmic loss is observed. No degradation is found in the anode performance under these conditions, which indicates that the changes on the cathode side have no significant effect on the anode side. Concentration overpotential was negligible before and after chromium poisoning. As chromium poisoning continues, the cathode ohmic loss linearly increases, whereas the cathode activation overpotential increases exponentially.

To further understand these trends, the distribution of the 1D average active TPB density and the

charge-transfer current density within the cathode are respectively shown in Figs. 4(a) and (b). Here, the TPB density and charge transfer current density at a given time are normalized by those under the initial conditions ($t = 0$), whose distributions are shown in Figs 4(a') and (b'), respectively. Fig. 5 shows the 3D distribution of the normalized TPB density and charge-transfer current density. Under the initial conditions without poisoning, since the resistance of the ion conduction is larger than that of the electron conduction, the electrode reaction takes place near the cathode–electrolyte interface. In this situation, the local activation overpotential also appears to be high near the interface, yielding a larger i_{D}. Therefore, as chromium poisoning continues, TPBs preferentially deteriorate from the cathode–electrolyte interface side. This gives a theoretical explanation of the degradation trends found in several experimental studies in the literature, where more chromium was found in the vicinity of the cathode–electrolyte interface. Also, as described in Eq. (16), the decrease in the TPB density near the interface increases activation overpotential there, and in spite of high resistance of ion conduction, the electrode reaction can take place even at the surface side. This elongates the ionic transport pathways within the cathode, resulting in an increase in the ohmic loss in the cathode.

4.2 Comparison with experimental studies

The relative decrease in the TPB density strongly depends on $P_{\mathrm{H_2O,Cr\,source}}$ because i_{D} and

$P_{\mathrm{CrO_2(OH)_2}}$ are affected by $P_{\mathrm{H_2O,Cr\,source}}$ as described in Eqs. (24) and (25). However, since steam is merely a minor impurity on the cathode side, the effects of steam on chromium poisoning were ignored in most studies. In addition, the relative decrease in the TPB density also depends on the initial TPB density and distribution. These factors preclude us from quantitative comparison with the experimental studies in the literature. Nevertheless, common trends exist in the dependence of the performance degradation rate on the cell temperature, the partial pressure of steam at the chromium source, the cathode microstructure, and the cathode thickness. In this study, we attempted to reproduce these trends of chromium poisoning using the proposed numerical model.

4.2.1 Effects of cell temperature

Taniguchi et al. [2] and Bentzen et al. [7] reported that a higher temperature prevents performance degradation in LSM-YSZ composite cathodes. By comparing the overpotentials in Cases 1 and 2 in Fig. 6, it was found that our simulation results can reproduce this tendency. One of the reasons for this is that the higher temperature increases $i_{0,\mathrm{cat}}$, which in turn decreases the local activation overpotential within the cathode, similar to the situation where the TPB density was increased in the previous subsection. Although a higher temperature also results in a higher $P_{\mathrm{CrO_2(OH)_2}}$ and may promote degradation due to chromium, the effect of the increase in $i_{0,\mathrm{cat}}$ is larger than that of the

increase in $P_{\mathrm{CrO_2(OH)_2}}$. From the simulation results, the relative increase in the activation overpotential over 1000 h, ($\eta_{\mathrm{act,cat}}(t{=}1000)$- $\eta_{\mathrm{act,cat}}(t{=}0)$)/$\eta_{\mathrm{act,cat}}(t{=}0)$, at 850 °C is 80% of that at 750 °C.

4.2.2 Effects of partial pressure of steam at chromium source

Bentzen et al. [7] and Chen et al. [8] reported that a higher $P_{\mathrm{H_2O,Cr\ source}}$ causes more severe degradation. Possible reasons for this are the fact that a higher $P_{\mathrm{H_2O,Cr\ source}}$ increases $P_{\mathrm{CrO_2(OH)_2}}$ and at the same time promotes the chromium oxide deposition reaction as can be seen from Eq. (25). By comparing the overpotentials in Cases 1 and 3 and in Cases 2 and 4 in Fig. 6, it was found that our simulation can reproduce this trend. Under the dry conditions, the relative increase in the activation overpotential was smaller than that under the wet conditions, the former being only 5.4 and 3.8%/1000 h in the LSM-YSZ composite cathode at 750 and 850 °C the letter being 290 and 230%/1000 h, respectively. Under practical conditions, where the cathode-side gas is ambient air, the molar fraction of steam can easily exceed 2.4%. Therefore, measures need to be taken to keep the humidity of the cathode air as low as possible to prevent chromium poisoning.

4.2.3 Effects of cathode microstructure

Konysheva et al. [6] reported that LSM-YSZ composite cathodes had higher tolerance to chromium poisoning than LSM cathodes. By comparing the overpotentials in Cases 1 and 5 in Fig. 6, it was found that our simulation reproduce this phenomenon. Since the activation overpotential can be reduced by a larger TPB density in the composite cathodes, the relative decrease in the TPB density in the LSM-YSZ composite cathodes is lower than that in the LSM cathodes. This implies that a cathode with a finer microstructure and a larger TPB density can further increase the tolerance of the electrodes to chromium poisoning. In other words, at a certain current density, the initial activation overpotentials determine the relative decrease in the TPB density because they reflect the initial TPB density in the microstructure.

4.2.4 Effects of cathode thickness

Konysheva et al. [6] also reported that in LSM-YSZ composite cathodes, the relative increase in the activation overpotential was larger in a thinner cathode. By comparing the overpotentials in Cases 7 and 8 in Fig. 7(a), it was found that the trends in experiments are also reproduced in the simulation results. A possible reason for the larger degradation in the thinner cathode is that active TPBs still remain even after 1000 h of operation in the case of a thicker LSM-YSZ composite cathode as shown in Fig. 7(b). The mechanism of this phenomenon can be explained as follows.

Chromium poisoning progresses faster in the vicinity of the cathode–electrolyte interface because of the higher local activation overpotential, and the electrochemically active region expands to the cathode surface to reduce the total activation overpotential. If this occurs, chromium poisoning begins to occur even in the surface region because of the electrochemical reaction there, which further reduces the TPB density. Once the area of chromium poisoning reaches the surface region, there is no other way to reduce the total activation overpotential, resulting in a rapid drop in performance of the LSM-YSZ composite cathodes. Because the total TPB density is larger in a thicker LSM-YSZ composite cathode, it takes longer for all the TPBs to be completely deactivated by chromium poisoning, which results in higher tolerance. This also implies that in planar SOFCs with chromium as an impurity, thinner parts lose their electrochemical activity more quickly, causing local decreases in temperature. Non-uniformity of the cathode thickness should also be avoided from the viewpoint of chromium poisoning.

5. Conclusions

A 3D numerical model of a single SOFC cell considering chromium poisoning on the cathode side has been developed to investigate the evolution of the SOFC performance over long-term

operation. The calculation domain consisted of an actual electrode microstructure obtained using an FIB-SEM. The simulation results revealed that the degradation by chromium is mainly caused by an increase in the cathode activation overpotential due to a decrease in the TPB length. In addition, in LSM-YSZ composite cathodes, TPBs near the cathode–electrolyte interface are preferentially deteriorated by chromium since the relative decrease in the TPB density increases with the higher local activation overpotential. This expands the active reaction region towards the cathode surface, also resulting in an increase in the ohmic loss. Furthermore, our simulation reproduced the trends of chromium poisoning observed in experiments in the literatures: (i) a higher temperature prevents degradation because it increases the exchange current density per unit TPB length and reduces the local activation overpotential, (ii) a higher partial pressure of steam at the chromium source causes faster degradation because chromium vapor formation is promoted at a higher steam concentration, (iii) LSM cathodes have lower tolerance to chromium than LSM-YSZ composite cathodes because the initial activation overpotential is larger in LSM cathodes than in LSM-YSZ composite cathodes, (iv) thicker LSM-YSZ composite cathodes have higher tolerance to chromium poisoning because they have larger active TPBs even after chromium poisoning. More quantitative validation of the proposed model will be possible when the effects of various operation conditions of SOFC systems on rate of chromium poisoning are clearly understood through more elaborate experiments. This will

enable the more reliable prediction of SOFC performance in long-term operation and should be attempted as future works.

Acknowledgment

This work was supported by the New Energy and Industrial Technology Development Organization (NEDO) under the Development of System and Elemental Technology for Solid Oxide Fuel Cell (SOFC) Project and by a Grant-in-Aid for JSPS Fellows. We also thank Mr. Y. Tanaka for helping us to construct the numerical model.

References

[1] H. Yokokawa, H. Tu, B. Iwanschitz, A. Mai, Fundamental mechanisms limiting solid oxide fuel cell durability, J. Power Sources 182 (2008) 400–412.

[2] S. Taniguchi, M. Kadowaki, H. Kawamura, T. Yasuo, Y. Akiyama, Y. Miyake, T. Saitoh, Degradation phenomena in the cathode of a solid oxide fuel cell with an alloy separator, J. Power Sources 55 (1995) 73–79.

[3] S.P. Jiang, J.P. Zhang, L. Apateanu, K. Foger, Deposition of chromium species at Sr-doped $LaMnO_3$ electrodes in solid oxide fuel cells. I. Mechanism and kinetics, J. Electrochem. Soc. 147 (11) (2000) 4013–4022.

[4] Y. Matsuzaki, I. Yasuda, Dependence of SOFC cathode degradation by chromium-containing alloy on compositions of electrodes and electrolytes, J. Electrochem. Soc. 148 (2001) A126–A131.

[5] E. Konysheva, H. Penkalla, E. Wessel, J. Mertens, U. Seeling, L. Singheiser, K. Hilpert, Chromium poisoning of perovskite cathodes by the ODS alloy $Cr_5Fe_1Y_2O_3$ and the high chromium ferritic steel Crofer22APU, J. Electrochem. Soc. 153 (2006) A765–A773.

[6] E. Konysheva, J. Mertens, H. Penkalla, L. Singheiser, K. Hilpert, Chromium poisoning of the porous composite cathode effect of cathode thickness and current density, J. Electrochem. Soc. 154 (2007) B1252–B1264.

[7] J.J. Bentzen, J.V.T. Høgh, R. Barfod, A. Hagen, Chromium poisoning of LSM/YSZ and LSCF/CGO composite cathodes, Fuel Cells 9 (2009) 823–832.

[8] X. Chen, Y. Zhen, J. Li, S.P. Jiang, Chromium deposition and poisoning in dry and humidified air at $(La_{0.8}Sr_{0.2})_{0.9}MnO_{3+\delta}$ cathodes of solid oxide fuel cells, Int. J. Hydrogen Energy 35 (2010) 2477–2485.

[9] T. Horita, D.-H. Cho, F. Wang, T. Shimonosono, H. Kishimoto, K. Yamaji, M.E. Brito, H. Yokokawa, Correlation between degradation of cathode performance and chromium concentration in (La,Sr)MnO_3 cathode, Solid State Ionics 225 (2012) 151–156.

[10] H. Yokokawa, T. Horita, N. Sakai, K. Yamaji, M.E. Brito, Y.-P. Xiong, H. Kishimoto, Thermodynamic considerations on Cr poisoning in SOFC cathodes, Solid State Ionics 177 (2006) 3193–3198.

[11] A. Nakajo, P. Tanasini, S. Diethelm, J.V Herle, D. Favrat, Electrochemical model of solid oxide fuel cell for simulation at the stack scale II: Implementation of degradation processes, J. Electrochem. Soc. 158 (2011) B1102–B1118.

[12] J.R. Wilson, W. Kobsiriphat, R. Mendoza, H.-Y. Chen, J.M. Hiller, D.J. Miller, K. Thornton, P.W. Voorhees, S.B. Adler, S.A. Barnett, Three-dimensional reconstruction of a solid-oxide fuel-cell anode, Nat. Mater. 5 (2006) 541–544.

[13] K. Matsuzaki, N. Shikazono, N. Kasagi, Three-dimensional numerical analysis of mixed ionic and electronic conducting cathode reconstructed by focused ion beam scanning electron microscope, J. Power Sources 196 (2011) 3073–3082.

[14] T. Carraro, J. Joos, B. Rüger, A. Weber, E. Ivers-Tiffee, 3D finite element model for reconstructed mixed-conducting cathodes: I. Performance quantification, Electrochim. Acta 77 (2012) 315–323.

[15] H. Iwai, N. Shikazono, T. Matsui, H. Teshima, M. Kishimoto, R. Kishida, D. Hayashi, K. Matsuzaki, D. Kanno, M. Saito, H. Muroyama, K. Eguchi, N. Kasagi, H. Yoshida, Quantification of SOFC anode microstructure based on dual beam FIB-SEM technique, J. Power Sources 195 (2010) 955–961.

[16] M. Kishimoto, H. Iwai, M. Saito, H. Yoshida, Three-dimensional simulation of SOFC anode polarization characteristics based on sub-grid scale modeling of microstructure, J. Electrochem. Soc. 159 (2012) B315–B323.

[17] M. Kishimoto, H. Iwai, K. Miyawaki, M. Saito, H. Yoshida, Improvement of the sub-grid-scale model designed for 3D numerical simulation of solid oxide fuel cell electrodes using an adaptive power index, J. Power Sources 223 (2013) 268–276.

[18] K. Miyoshi, T. Miyamae, H. Iwai, M. Saito, M. Kishimoto, H. Yoshida, Exchange current model for $(La_{0.8}Sr_{0.2})_{0.95}MnO_3$ (LSM) porous cathode for solid oxide fuel cells, J. Power Sources, submitted.

[19] M. Kishimoto, M. Lomberg, E. Ruiz-Trejo, N.P. Brandon, Enhanced triple-phase boundary density in infiltrated electrodes for solid oxide fuel cells demonstrated by high-resolution tomography, J. Power Sources 266 (2014) 291–295.

[20] M. Kishimoto, M. Lomberg, E. Ruiz-Trejo, N.P. Brandon, Numerical modeling of nickel-infiltrated gadolinium-doped ceria electrodes reconstructed with focused ion beam tomography, Electrochim. Acta 190 (2016) 178–185.

[21] E.A. Mason, A.P. Malinauskas, Flow and diffusion of gases in porous media, J. Chem. Phys. 46 (1967) 3199–3216.

[22] J.R. Ferguson, J.M. Fiard, R. Herbin, Three-dimensional numerical simulation for various geometries of solid oxide fuel cells, J. Power Sources 58 (1996) 109–122.

[23] Y. Ji, J. Kilner, M. Carolan, Electrical properties and oxygen diffusion in yttria-stabilised zirconia (YSZ)–$La_{0.8}Sr_{0.2}MnO_{3\pm\delta}$ (LSM) composites, Solid State Ionics 176 (2005) 937–943.

[24] J.H. Park, R.N. Blumenthal, Electronic transport in 8 mole percent Y_2O_3-ZrO_2, J. Electrochem. Soc. 136 (1989) 2867–2876.

[25] N.F. Bessette II, W.J. Wepfer, J. Winnick, A mathematical model of a solid oxide fuel cell, J. Electrochem. Soc. 142 (1995) 3792–3800.

[26] J.H. Nam, D.H. Jeon, A comprehensive micro-scale model for transport and reaction in intermediate temperature solid oxide fuel cells, Electrochim. Acta 51 (2006) 3446–3460.

[27] U. Anselmi-Tamburini, G. Chiodelli, M, Armondi, F. Maglia, G. Spinolo, Z.A. Munir, Electrical properties of Ni/YSZ cermets obtained through combustion synthesis, Solid State Ionics 110 (1998) 35–43.

[28] S. Nagata, A. Momma, T. Kato, Y. Kasuga, Numerical analysis of output characteristics of tubular SOFC with internal reformer, J. Power Sources 101 (2001) 60–71.

[29] T. Kawada, N. Sakai, H. Yokokawa, M. Dokiya, M. Mori, T. Iwata, Characteristics of slurry-coated nickel zirconia cermet anodes for solid oxide fuel cells, J. Electrochem. Soc. 137 (1990) 3042–3047.

[30] Y. Suzue, N. Shikazono, N. Kasagi, Micro modeling of solid oxide fuel cell anode based on stochastic reconstruction, J. Power Sources 184 (2008) 52–59.

[31] K. Hilpert, D. Das, M. Miller, D.H. Peck, R. Weiß, Chromium vapor species over solid oxide fuel cell interconnect materials and their potential for degradation processes, J. Electrochem. Soc. 143 (1996) 3642–3647.

[32] B.B. Eddinghaus, Thermodynamics of gas phase chromium species: the chromium oxides, the chromium oxyhydroxides, and volatility calculations in waste incineration processes, Combust. Flame 93 (1993) 119–137.

[33] L.G.J. de Haart, J. Mougin, O. Posdziech, J. Kiviaho, N.H. Menzler, Stack degradation in dependence of operation parameters; the real-SOFC sensitivity analysis, Fuel cells 9 (2009) 794-804.

[34] A. Bertei, C. Nicolella, Dusty-gas model with uniform pressure: a numerical study on the impact of a frequent inconsistent assumption in SOFC electrode modeling, ECS Transactions 68 (2015) 2887-2895.

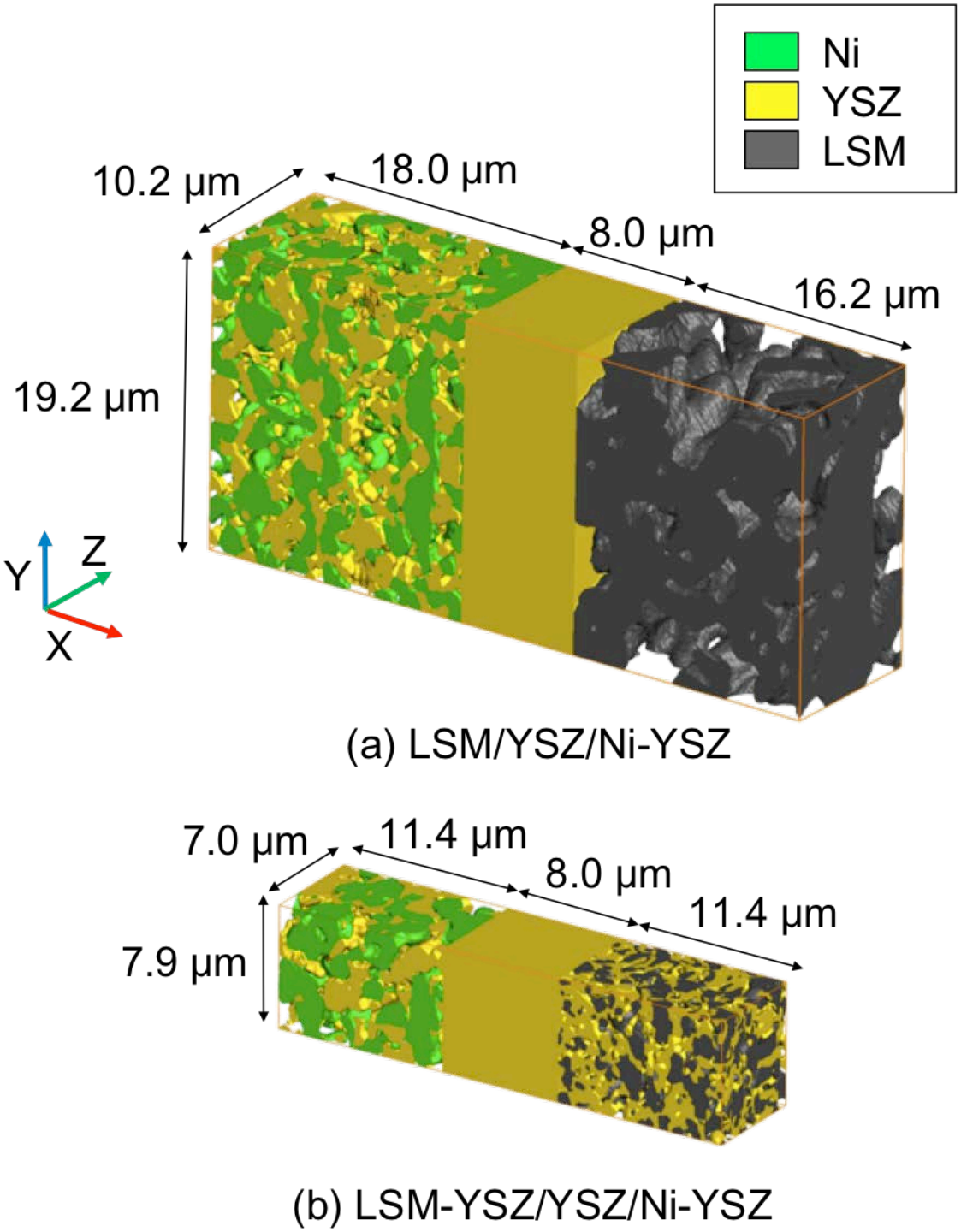

Fig. 1 Schematic image of the calculation domains. (a) LSM/YSZ/Ni-YSZ and (b) LSM-YSZ/YSZ/Ni-YSZ.

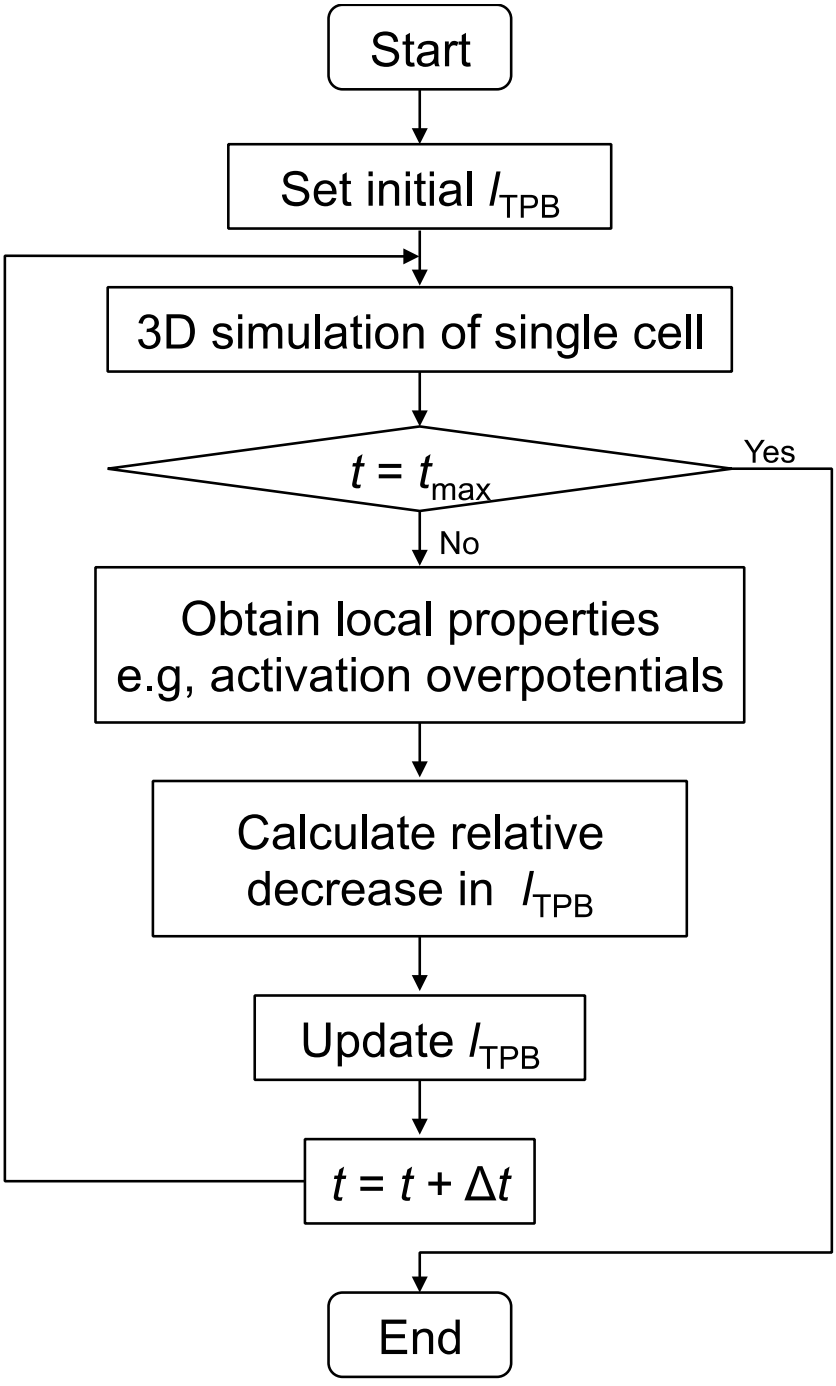

Fig. 2 Flowchart of the chromium poisoning simulation.

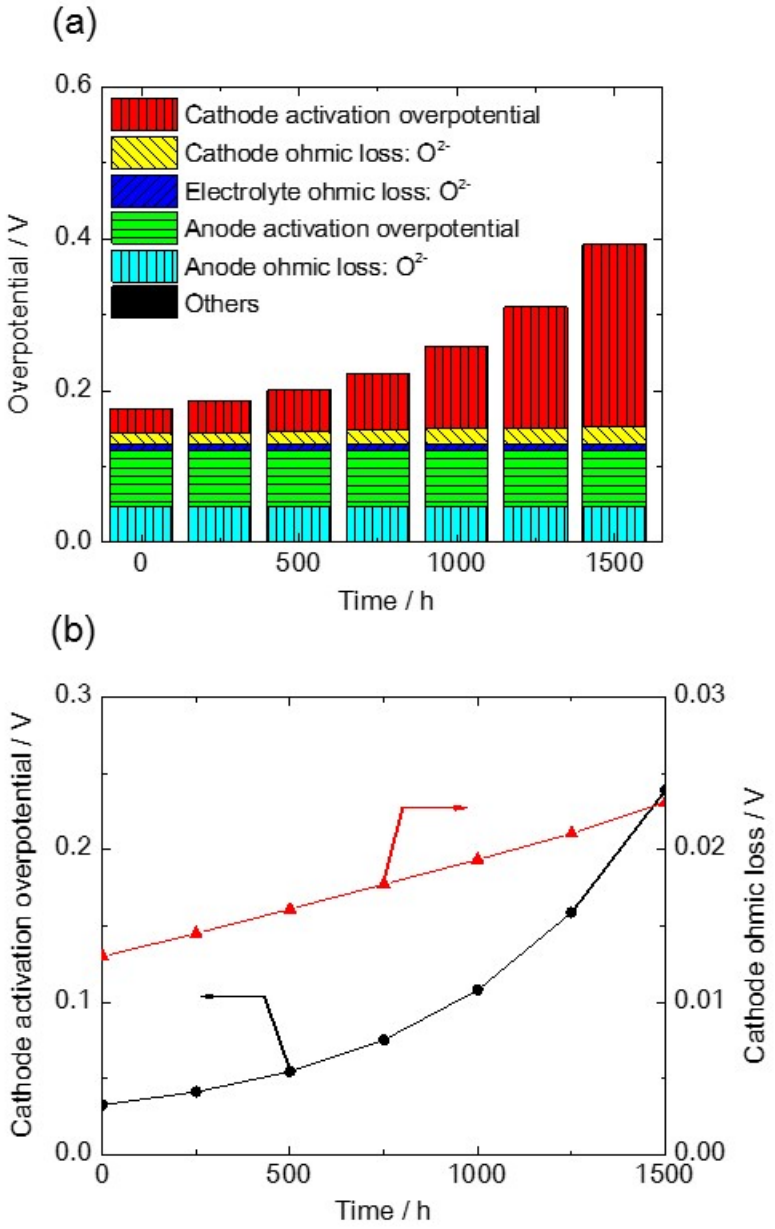

Fig. 3 Time evolution of (a) voltage losses of the single cell and (b) cathode activation overpotential and ohmic loss.

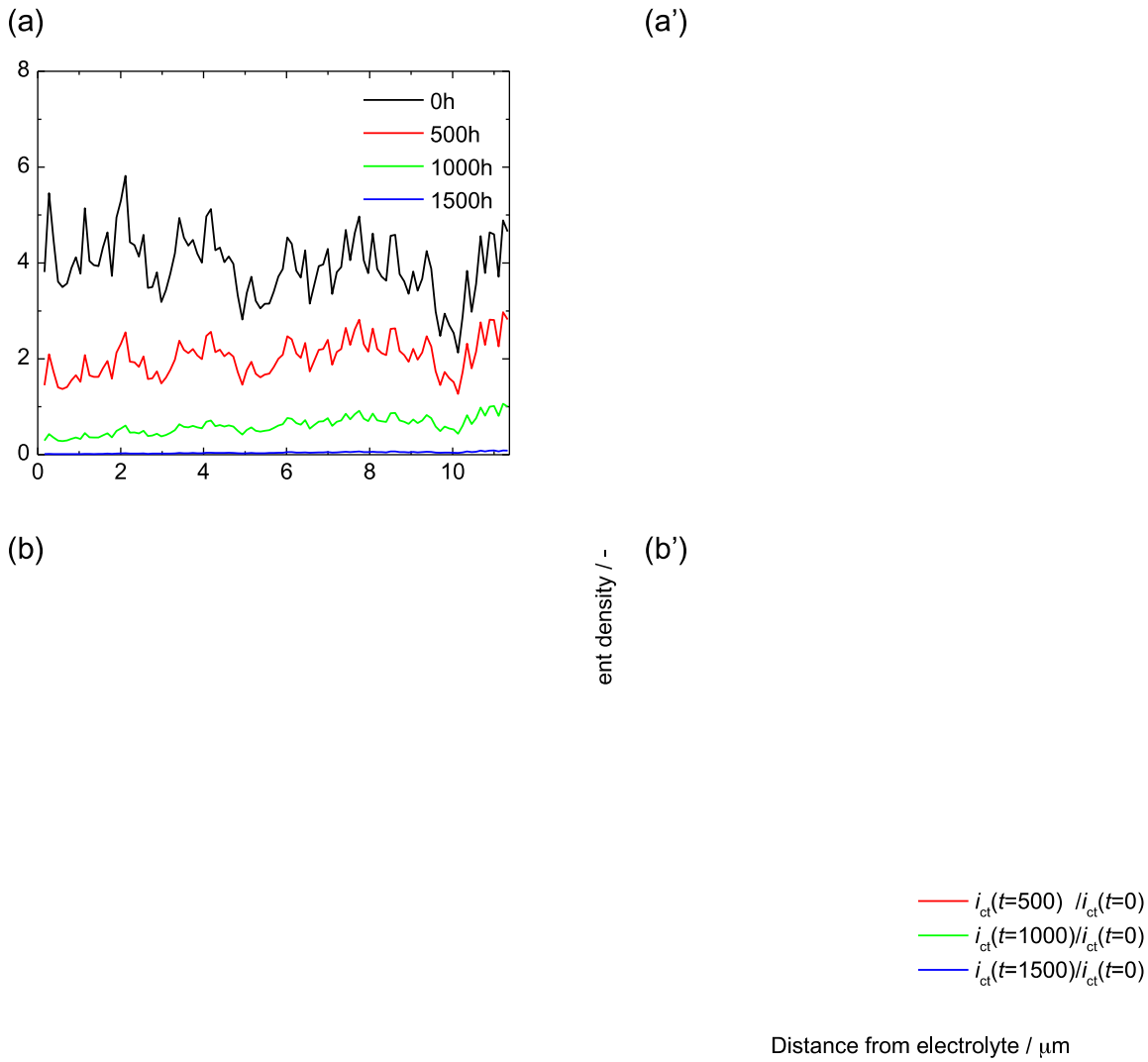

Fig. 4 Time evolution of (a) 1D average TPB density, (a') normalized TPB density $l_{TPB}(t)/l_{TPB}(t=0)$, (b) 1D average charge-transfer current density, and (b') normalized charge-transfer current density $i_{ct}(t)/i_{ct}(t=0)$.

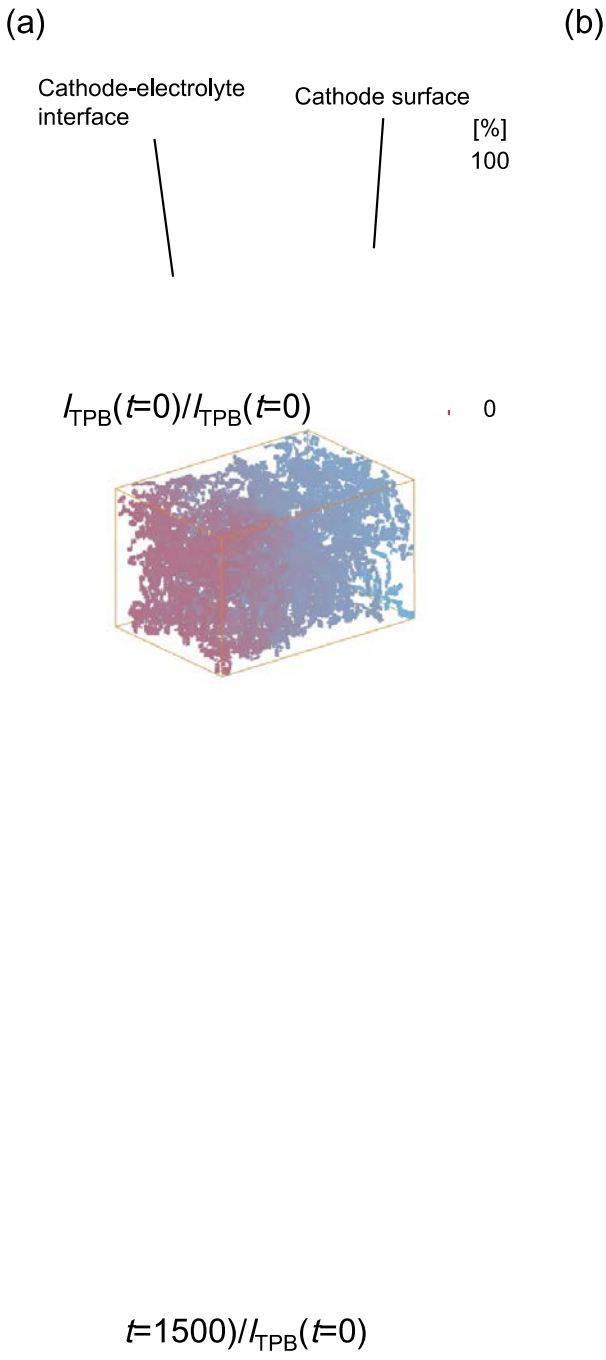

Fig. 5 3D distribution of (a) normalized TPB density $l_{TPB}(t)/l_{TPB}(t=0)$ and (b) charge-transfer current density i_{ct}.

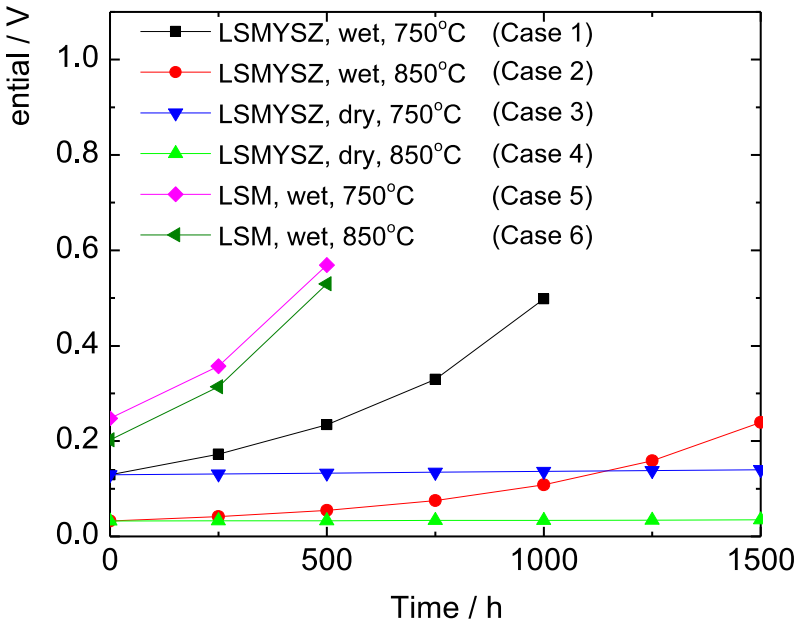

Fig. 6 Cathode activation overpotentials in LSM and LSM-YSZ composite cathodes at 750 and 800 ºC.

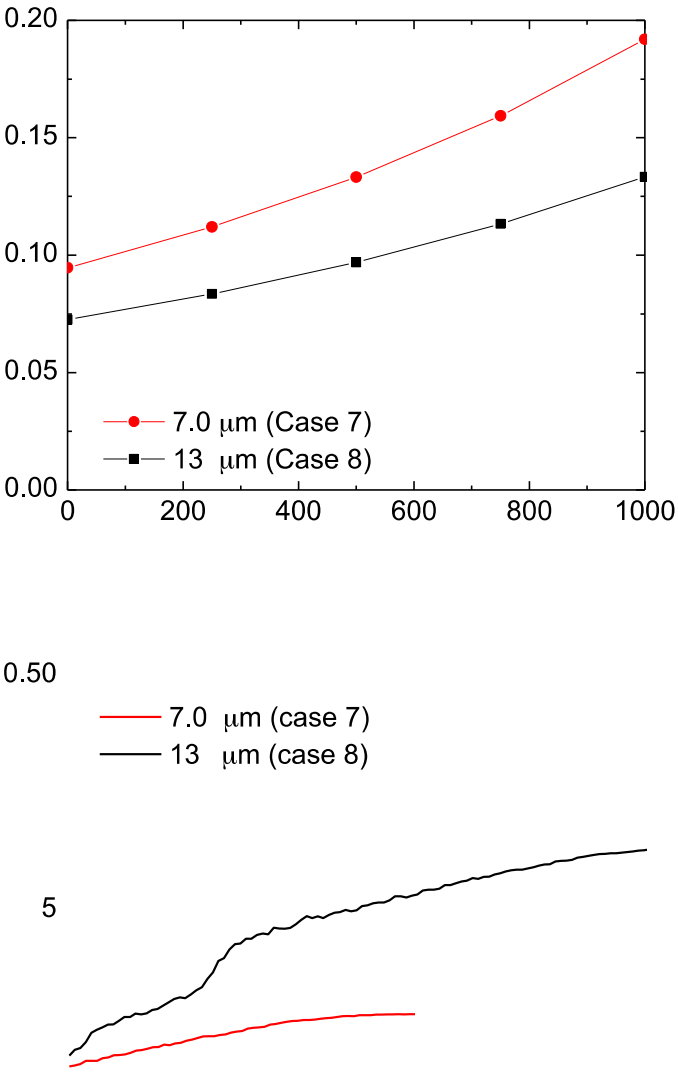

Fig. 7 (a) Cathode activation overpotential as a function of time. (b) Normalized TPB density $l_{TPB}(t=1000)/l_{TPB}(t=0)$.